




Morphology of cross-linked cellulose nanocrystal aerogels: cryo-templating versus pressurized gas expansion processing

Daniel A. Osorio¹, Bernhard Seifried², Paul Moquin², Kathryn Grandfield¹, and Emily D. Cranston^{3,*} 

¹Department of Materials Science and Engineering, McMaster University, 1280 Main Street West, Hamilton, ON L8S 4L7, Canada

²Ceapro Inc., 7824 - 51 Avenue NW, Edmonton, AB T6E 6W2, Canada

³Department of Chemical Engineering, McMaster University, 1280 Main Street West, Hamilton, ON L8S 4L7, Canada

Received: 17 December 2017

Accepted: 16 March 2018

Published online:
29 March 2018

© Springer Science+Business Media, LLC, part of Springer Nature 2018

ABSTRACT

Cellulose nanocrystal (CNC)-based aerogels are often produced through cryo-templating, followed by either critical point drying or freeze drying. While cryo-templating gives aerogels with a bimodal pore size distribution, better morphological control may be needed for certain applications. This work compares CNC aerogels prepared using a new processing method, called pressurized gas expansion (PGX) technology, to aerogels produced via cryo-templating. In all cases, CNCs were surface-modified with orthogonal functional groups to produce covalently cross-linked aerogels which are flexible and do not disperse in water. The aerogels were imaged by scanning electron microscopy and X-ray micro-computed tomography and further characterized by nitrogen sorption isotherms, X-ray diffraction, X-ray photoelectron spectroscopy, and compression testing. PGX aerogels appeared expanded and fibrillar at high magnification, with small mesopores and macropores less than 7 μm , but with large mound-like porous aggregates. Conversely, cryo-templated aerogels were comprised of denser CNC sheets surrounding macropores of 10–950 μm . Overall, PGX aerogels had a lower density, higher porosity, and a higher specific surface area than cryo-templated aerogels; they were also less stiff due to their morphology and reduced number of chemical cross-links. Scale-up of aerogel processing and understanding of the tunability of such methods may extend the use of CNCs in applications including insulation, separations, flexible supports, drug delivery, and template materials.

Address correspondence to E-mail: ecranst@mcmaster.ca

Introduction

Aerogels are dry ultra-low-density materials derived from gel networks by replacing the liquid medium with gas [1]. Aerogels are lightweight with porosities over 99% [1] and have become popular in a variety of applications, such as acoustic and thermal insulation, energy production/storage, membrane separations, CO₂ capture, and catalyst supports [2]. Silica aerogels are the most commonly studied aerogels and are readily available commercially. While they have been praised for their insulating abilities and porosity, they have been criticized for their brittle and fragile properties [2]. To overcome this limitation, alternative aerogel starting materials have been investigated, such as polymers [3], carbon nanotubes [4, 5], graphene [6], nanoclays [7], and nanocellulose [8, 9], in order to produce aerogels that are more mechanically robust.

Nanocellulose is a nanoscale derivative of natural cellulose, namely cellulose nanofibrils (CNFs) and cellulose nanocrystals (CNCs); both have been used to produce cellulose-based aerogels as well as composites, emulsions, coatings, and packaging materials [10]. CNFs are isolated primarily through mechanical processes, sometimes combined with chemical/enzymatic pretreatments, which generates ca. 5 nm wide and up to several micrometers long fibrils that consist of ordered and disordered cellulose regions, making them relatively flexible [11]. As such, CNFs entangle easily at low concentrations which allows them to form highly porous gel networks with good mechanical properties [12]. On the other hand, CNCs are highly crystalline and rigid rod-shaped particles that have diameters of 5–10 nm and lengths of 100–200 nm (when produced from wood and cotton [13]) and therefore have a limited ability to “entangle.” Both CNFs and CNCs are renewably sourced, non-toxic [14], and easily functionalized through well-known surface chemistry [15]. We employ this latter property to add cross-linking groups to the CNC surface to allow them to covalently form a networked structure providing us with control over the internal aerogel structure and ensuring the final materials do not redisperse in liquid environments.

CNCs are most commonly extracted by acid hydrolysis or oxidation and have specific surface areas ranging from 200 to 500 m² g⁻¹ [16, 17]. Their high rigidity and surface area have been exploited in

the literature to create CNC aerogels with potential across a broad range of applications such as supercapacitor electrode supports [18], selective absorbents [19], and thermal insulators [20]. Compared to silica aerogels, CNC aerogels have similar ultra-low density, high porosity, and high specific surface area but with the important advantage of being mechanically strong and flexible [12].

The first CNC aerogels reported were held together by weak cellulose–cellulose interactions (e.g., hydrogen bonding and van der Waals forces [12]); however, they redispersed in aqueous environments, losing their porous gel structure [21]. More recently, this has been remedied by covalently binding CNCs together using various cross-linking chemistries [22–24]. Our group previously showed that hydrazone bonds could be formed between CNCs that were surface-modified with aldehyde and hydrazide groups and the aerogels produced had shape recovery properties, even when submerged in water [25]. The hydrazone cross-linking is based on bio-orthogonal functional groups that react immediately when in contact, such that external stimuli or additional chemicals are not needed; furthermore, the chemistry is suitable for biomedical applications and the gelation kinetics and cross-link degradation have been well documented [26].

There are some advantages of CNC aerogels over CNF aerogels, but the ultimate properties and applications will dictate the ideal nanocellulose type and production method needed. Specifically, the aerogels produced in this work rely solely on chemical cross-links to hold CNCs together. CNF aerogels, on the other hand, are based on physical entanglements sometimes combined with chemical cross-links [12]. As such, CNCs allow for more control over mechanical properties and porosity since CNCs and the cross-linking chemistry used here are rigid compared to the more flexible CNFs [25]. Furthermore, CNC aerogel degradation can be tailored unlike with entangled CNF aerogels. The chemical purity, higher specific surface area, and lower size polydispersity (uniformity) of CNCs compared to CNFs may also play a key role for some target areas, such as biomedical applications.

CNC aerogels with a variety of surface chemistries and functionality have been described in the literature and are mostly produced using freeze drying or a combination of freezing followed by critical point drying (CPD), which are both cryo-templating

methods [12]. Freezing induces a gel or networked structure that can also be achieved, in some cases, through solvent exchange alone, and as such, CNC aerogels from CPD without freezing have been demonstrated [27]. Generally, however, nanocellulose aerogels produced by CPD have included both freezing and solvent exchange steps; however, they are not strictly necessary in all cases. To the best of our knowledge, there have been no reports focused on CNC aerogel processing methods, and as such, this work sets out to compare cryo-templated CNC aerogels and a new industrial-scale drying method called pressurized gas expansion (PGX) technology.

Cryo-templating is the process used here to freeze a suspension of CNCs in water to form ice crystals. As ice crystals grow, they exclude the CNCs from the water phase, forcing CNCs together into sheet-like structures. In our case, aldehyde- and hydrazide-modified CNCs form hydrazone bond when they come into contact and the CNCs become covalently tethered together [25]. More specifically, when the CNC suspension is frozen, it becomes a cryo-gel, and when intended for CPD, it is submerged into ethanol to solvent exchange the water as it melts, to become an alco-gel. The alco-gel is then subjected to CPD, which first solvent exchanges ethanol for supercritical CO₂ [25]. The supercritical CO₂ is then gradually depressurized to ambient conditions to create an aerogel. Similar to CPD, CNC aerogels have also been prepared by freeze drying [28–30] (and directional freeze drying [31]) where the cryo-gel is subjected to a low temperature high vacuum, which causes the ice crystals to sublime producing an aerogel. Both processing methods lead to similar aerogel morphologies with stacked CNC sheets separated by macropores. Mesopores (2–50 nm in diameter) can be found between individual CNCs on each sheet [25]. While both methods give highly porous and reproducible aerogel morphologies, the multiple steps and time-consuming solvent exchanges (required in CPD with CNCs to avoid collapse if processed directly from water) may limit the scale-up of these aerogel production routes.

PGX technology is a potential new scalable tool for aerogel processing [32–35]. In our application, the PGX technology consisted of mixing an existing “loose” CNC gel network in water and ethanol, pumping it into a pressurized vessel through a coaxial nozzle where it is exposed to a turbulent regime of PGX liquids consisting of anhydrous

ethanol and supercritical carbon dioxide (CO₂). This violent encounter with the PGX liquid causes a rapid and homogenous dehydration while preserving the original CNC gel network, which remains intact upon depressurization. Industrially, the PGX technology is used to simultaneously extract, purify, micronize, and dry (bio)polymers/nanoparticles intended for cosmeceutical, nutraceutical, and therapeutic products. The main parameters that impact the morphology of PGX dried materials are: the initial nature of the polymers/particles, the concentration (with possible addition of ethanol), and the feed flowrates, which can affect turbulence in the nozzle, precipitation, and dehydration rates inside the vessel.

Our study aims to explore PGX to produce aerogels and to assess its potential as a scalable process for the manufacture of chemically cross-linked CNC aerogels. Hence, this paper compares two types of chemically cross-linked CNC aerogels—one produced through the PGX process and the other produced through the cryo-templating process. The aerogels were thoroughly characterized to understand the morphologies attainable through the different processing routes. Specific surface area, pore size distribution, mechanical properties, chemical cross-link density, crystallinity, and microstructure were investigated.

Materials and methods

Materials

Whatman cotton ashless filter aid was purchased from GE Healthcare Canada (Mississauga, Canada). Sulfuric acid (95–98%) and dimethyl sulfoxide were purchased from Caledon Laboratory Chemicals (Georgetown, Canada). Anhydrous ethanol was purchased from Commercial Alcohols (Toronto, Canada). 2,2,6,6-(tetramethylpiperidin-1-yl)oxyl (TEMPO, 99% purified by sublimation), adipic acid dihydrazide (ADH) $\geq 98\%$, *N*'-ethyl-*N*-(3-(dimethylamino)propyl)-carbodiimide (EDC, commercial grade), ethylene glycol (99.8%), silver(I) oxide (Ag₂O, $\geq 99.99\%$ trace metals basis), sodium periodate (NaIO₄, $> 99.8\%$), *N*-hydroxysuccinimide (NHS, 97%), sodium hypochlorite solution (NaClO, 10–15%), sodium bromide (NaBr, Reagent Plus[®] $\geq 99\%$), and thiocarbonylhydrazide (TCH) 98% were purchased from Sigma-Aldrich (Oakville, Canada).

Osmium tetroxide (OsO_4) solution was purchased from Canemco & Marivac (Lakefield, Canada). Hydrochloric acid (HCl, 0.1 M and 1 M) and sodium hydroxide (NaOH, 0.1 and 1 M) were purchased from LabChem Inc. (Zelienople, USA). All water used was purified type I water with a resistivity of 18.2 M Ω cm (Barnstead NANOpure Diamond system, Thermo Scientific, Asheville, USA). No chemicals were modified or further purified before use.

Preparation of cellulose nanocrystals (CNCs)

CNCs were prepared through sulfuric acid hydrolysis, as described previously [13]. Briefly, cotton ashless filter aid (40 g) was first blended into a cotton pulp. The pulp was added to 700 mL of 64 wt% sulfuric acid and hydrolyzed for 45 min at 45 °C under constant mechanical stirring. The cotton acid slurry was then added to 7 L of 4 °C purified water to quench the reaction, and was left for 1 h to settle. The slurry was then subjected to multiple 10-min rounds of centrifugation at 5000 rpm. The slurry was centrifuged until a pellet no longer formed. The CNC suspension was then dialyzed against purified water using dialysis membranes with a 14 kDa molecular weight cutoff (Sigma-Aldrich). Dialysis water was changed daily for 2 weeks until the pH of the dialysis water no longer changed (ca. pH 5–6). The CNC suspension was then probe-sonicated (Sonifier 450, Branson Ultrasonics, Danbury, USA) in an ice bath for three individual rounds (15 min total) at an output energy of 60%. The CNC suspension was then passed through Whatman glass microfiber filter paper and stored at 4 °C. CNCs produced using sulfuric acid hydrolysis have grafted sulfate half-ester groups on their surface that impart an anionic surface charge and colloidal stability in water [13]; in this case, CNCs were stored in suspension in the acid form, meaning the counterion on the sulfate half-ester is a proton.

Aldehyde CNC (CHO–CNC) modification

To add aldehyde groups onto the CNC surfaces, 20 g of NaIO_4 was added to 500 mL of a 1 wt% CNC suspension in a 1-L round-bottom flask [36]. The flask was completely covered in aluminum foil to protect the NaIO_4 from light. After the NaIO_4 was dissolved, the pH of the suspension was lowered to 3.5 ± 0.2

with 1 M HCl. The round-bottom flask was then covered with a septum and placed in a $45 \text{ °C} \pm 0.1 \text{ °C}$ oil bath (the oil bath was also wrapped in aluminum foil) under constant stirring for 4 h. Subsequently, the suspension was removed from the oil bath and 10 g of ethylene glycol was added to quench the reaction. The suspension was also exposed to light and air to assist in quenching the reaction. After 10 min, the reaction was considered quenched and dialyzed for two weeks with daily water changes. CHO–CNCs were stored at 4 °C.

Carboxylic acid CNC (COOH–CNC) modification

To add carboxylic acid groups onto the CNC surfaces, a TEMPO oxidation reaction was performed [15, 37]. A 200 mL solution containing 0.148 g of TEMPO and 1.62 g of NaBr was slowly added drop-wise to 500 mL of a 1 wt% CNC suspension in a 1-L round-bottom flask at ambient conditions with stirring. Immediately after, 30 g of 12.5 wt% NaClO was slowly added to the suspension drop-wise. The suspension was allowed to react for 3 h. The pH of the reaction was closely monitored and maintained at 10 ± 0.2 with 1 M NaOH. After 3 h, 18.2 g of ethanol was added to the suspension to quench the reaction, which was then stirred for another 10 min. The suspension was then centrifuged for one round at 10,000 rpm and then dialyzed for 2 weeks with daily water changes. COOH–CNCs (in the sodium form) were stored at 4 °C.

Hydrazide CNC (NH_2NH –CNC) modification

The procedure by Yang and Cranston was used to add hydrazide groups onto the COOH–CNC surfaces [25]. Adipic acid dihydrazide (0.6 g) was added to 200 mL of a 1 wt% suspension of COOH–CNCs and allowed to dissolve. Both NHS and EDC were suspended in separate 1 mL 1:1 dimethyl sulfoxide/water solutions. The NHS and EDC solutions were then added to the CNC suspension, drop-wise and sequentially. The pH of the suspension was adjusted to 6.8 with NaOH and HCl until there was no more rapid pH change. The CNC suspension was then dialyzed for 2 weeks with daily water changes. NH_2NH –CNCs (in sodium form) were stored at 4 °C.

Degree of functionalization

Sulfate half-ester [38], aldehyde [39], carboxylic acid, and hydrazide content [25] on CNCs were quantified by conductometric titrations, as reported in the literature. A known mass of CNCs (12–15 mg dry) was added to 60 mL of purified water with 0.3 mL of 200 mM NaCl solution to achieve measurable conductivity readings. For titrations involving carboxylic acid content, 0.3 mL of 0.1 M HCl was added to the CNC suspension prior to titrating. This was used to gain a measurable slope for the titration curve as outlined in the literature [40]. Sulfate half-ester content was titrated using 0.250 mL aliquots of 2 mM NaOH. To ensure all surface acid groups could be titrated (i.e., were in acid form as opposed to sodium form), all functionalized CNCs were passed through ion exchange resin (Dowex® Marathon™ C hydrogen form, Sigma-Aldrich) before titration as outlined by Beck et al. [38]. Aldehyde, carboxylic acid, and hydrazide content were titrated using 0.05 mL aliquots of 10 mM NaOH. Since hydrazide groups are grafted to carboxylic acid groups, the carboxylic content remaining on $\text{NH}_2\text{NH-CNCs}$ was subtracted from the carboxylic content on COOH-CNCs to quantify the number of hydrazide groups on the $\text{NH}_2\text{NH-CNC}$ surface. Aldehyde content was measured by selectively oxidizing aldehyde groups into carboxylic acid groups with an Ag_2O oxidation reaction [39] by adding 0.193 g of Ag_2O and 0.027 g of NaOH to a 20 mL 0.25 wt% suspension of CHO-CNCs and allowing it to stir overnight. The reaction was then filtered through Whatman glass microfiber filter paper. All titrations were performed over a period of approximately 1 h in triplicate, and error intervals reported are standard deviations.

Cryo-templated CPD aerogel processing

Cryo-templated CPD aerogels were made by combining 2.5 mL of 2 wt% CHO-CNC suspension, 2.5 mL of 2 wt% $\text{NH}_2\text{NH-CNC}$ suspension, 0.5 mL of 200 mM NaCl, and 4.5 mL of purified water to create a 1 wt% suspension of $\text{CHO-CNC/NH}_2\text{NH-CNCs}$. This suspension was then vortexed for 2 min (level 10 Analog Vortex Mixer, VWR, Mississauga, Canada). Suspensions were then transferred into 15-mm-diameter or 8-mm-diameter shell vials (depending on the intended characterization). Vials were placed in a freezer at -4°C and allowed to freeze

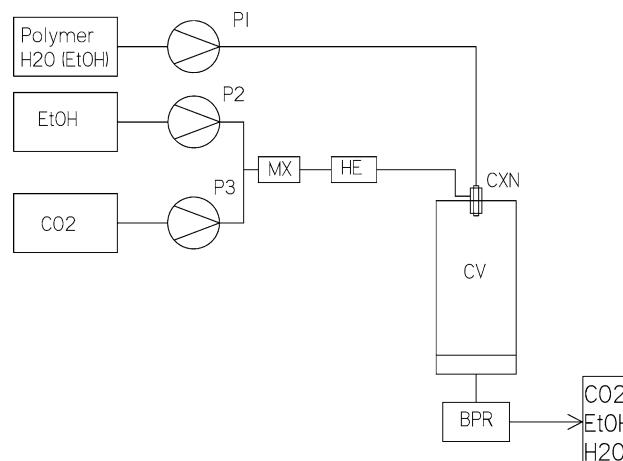


Figure 1 The simplified PGX process. P1/P2/P3 = positive displacement feed pumps; MX = static mixer; HE = heat exchanger; CXN = coaxial nozzle; CV = collection vessel; BPR = backpressure regulator.

overnight to form cryo-gels. The cryo-gels were transferred into anhydrous ethanol in ambient conditions. (No collapse of the gel structure was visible which implied that sequential solvent exchanges with increasing ethanol content were unnecessary.) Ethanol was changed every day for 5 days until the cryo-gels were fully infiltrated with ethanol, forming alco-gels. Finally, the alco-gels were transferred into a critical point dryer (Leica EM CPD300, Vienna, Austria), where ethanol was removed with supercritical CO_2 and gradually depressurized to ambient conditions for 2 h. All characterization was carried out on cryo-templated aerogels made from the same batch of CHO-CNCs and $\text{NH}_2\text{NH-CNCs}$.

Pressurized gas expansion (PGX) aerogel processing

PGX aerogels were processed at Ceapro Inc. in Edmonton, AB, Canada, using their patented technology. The simplified PGX process is shown schematically in Fig. 1 and has been described in detail previously [32]. Briefly, the experimental laboratory-scale system for PGX processing consisted of three positive displacement feed pumps (P1/P2/P3), a static mixer (MX), a heat exchanger (HE), a coaxial nozzle (CXN), a collection vessel (CV), and a backpressure regulator (BPR). The vessel was first pressurized with CO_2 and ethanol to 100 bar at 40°C utilizing P1 and P2 followed by the MX and HE to

reach a homogeneous single-phase mixture. Then, while pumping continuously, the CO₂ and ethanol mixture and the CNC slurry were introduced concurrently into the CV utilizing the CXN, which led to rapid mixing and three main “mechanisms” relevant for particle formation, described further in the Results and Discussion section. After the CNC slurry was injected, residual water and ethanol were flushed out using pure CO₂ at 100 bar and 40 °C. Once all water and ethanol were completely removed, a CNC network suspended in supercritical CO₂ remained, and then the system was returned to ambient pressure, thereby allowing CO₂ to change from the supercritical to the gas phase and exit the vessel without affecting the particle network structure [32, 35, 41].

More specifically, in our experiments a CNC slurry in ethanol and water was prepared prior to feeding it into the PGX system. Aqueous CHO–CNC and NH₂NH–CNC suspensions (1 wt%) were individually solvent-exchanged with anhydrous ethanol using stirred cell ultrafiltration (Millipore ultrafiltration system operated at 20–30 psi). The solvent exchange was stopped when a 9:1 ethanol/water ratio was obtained. 100 g of each CNC type in 90% ethanol was mixed together with an additional 100 g of anhydrous ethanol giving a total of 300 g to be used for PGX processing. The resulting mixture formed a gel that was stirred under high shear mixing with a Silverson L4RT-A with an Emulsor Screen attachment (Silverson Machines Inc., East Longmeadow, USA) at 3000 rpm for 3 min. This CNC ethanol–water slurry was then pumped into the PGX vessel through the CXN having a 0.152 inch internal diameter orifice size, using a custom Ceapro-built high-pressure pump at a feed flowrate of 20 g/min of CNC slurry containing 0.65 ± 0.02% CNCs. During CNC injection, the feed flowrates of CO₂ and ethanol were 21 and 42 g/min, respectively. A membrane filter with 5 μm pores was used to collect CNCs at the bottom of the 5-L collection vessel during PGX processing.

At the end of the process, one large aerogel was removed from the vessel as a uniform and dry material. The PGX processing method was used to produce five separate batches of highly consistent PGX aerogels; however, all aerogel characterization was carried out on the same PGX batch to show reproducibility within the batch and errors reported are between measurements on multiple samples.

As a control experiment, the CNC ethanol–water slurry (un-sheared) used in the PGX process was directly subjected to critical point drying without freezing or further solvent exchanges using the CPD equipment described above. A dense material that did not resemble an aerogel was obtained.

Viscosity measurements

Viscosity of the CNC ethanol–water slurry (i.e., the PGX feed) was measured using a Cannon–Fenske viscometer tube (size 200) for the thick slurry and a Cannon–Fenske viscometer tube (size 50) for the thinned CNC slurry. The viscometer tube was submerged in a 25 °C water bath. The CNC slurry was then allowed to pass through the viscometer’s marked start point and end point while being timed with a stopwatch. Equation 1 was used to calculate the viscosity of the sample where η_{ref} is the viscosity of the reference material, ρ_{ref} is the density of the reference material, ρ_{sample} is the density of the sample, t_{sample} is the time it took for the sample to flow through the viscometer, t_{ref} is the time it took for the reference material to flow through the viscometer, and η_{sample} is the viscosity of the sample. Anhydrous ethanol was used as the reference material for both CNC slurries. Viscosity measurements and the standard deviation were calculated over three separate individual sample measurements.

$$\eta_{\text{sample}} = \frac{\eta_{\text{ref}} * \rho_{\text{sample}}}{\rho_{\text{ref}}} * \frac{t_{\text{sample}}}{t_{\text{ref}}} \quad (1)$$

Dynamic light scattering (DLS)

DLS was used to determine a relative apparent particle size for CNCs in suspension. The term “apparent” is used in recognition of the fact that CNCs are rod-shaped particles and DLS assumes spherical particles [42]; nonetheless, we consider this a valid method to obtain relative sizes of neat and modified CNCs but the values should not be taken as absolute and do not represent either the length or the cross section of the CNCs. Measurements were taken on CNC suspensions diluted to 0.025 wt% with 10 mM NaCl added (to screen the electrostatic double layer) using a Malvern Zetasizer Nano particle analyzer (Malvern Instruments Ltd, Malvern, UK). Particle size readings were obtained over 11 measurements for each of three separate samples with the

temperature maintained at 23 °C. Standard deviation was calculated from three individual sample measurements.

Zeta potential

The zeta potential of CNC samples was measured using a ZetaPlus electrophoretic mobility analyzer (Brookhaven Instruments Corp, Holtsville, USA). Samples were prepared by diluting CNC suspensions to 0.25 wt% and adding 10 mM NaCl (to ensure accurate and comparable zeta potential values) [43]. Zeta potential values were taken from an average of 10 measurements of 15 cycles per sample, all at 23 °C. Standard deviation was calculated from three individual sample measurements.

Density calculation

The aerogel densities were determined by measuring the mass of the aerogel (Analytical Balance, Mettler, readability of 0.0001 g) and dividing it by the measured volume (calculated from dimensions measured with a digital calliper). Diameter and height measurements were calculated as an average of five measurements taken at five different locations on the aerogel. Four aerogels were used to determine the average density of each type of aerogel. Mass values for all CNC aerogels were measured in ambient conditions; we acknowledge that the mass values calculated could be possibly skewed due to water adsorbing within the high surface area aerogels.

The density of CNC ethanol–water slurries (i.e., the PGX feed) was measured by weighing the mass of a 1 mL of sample. Similarly for the critically point-dried CNC slurry control, the mass of approximately 0.5 mL was measured.

Porosity calculations

The aerogel porosities were calculated using Eq. 2 from the literature [25].

$$P(\%) = 100 * \left(1 - \frac{\rho_{\text{Gel}}}{\rho_{\text{CNC}}} \right) \quad (2)$$

where P is the porosity of the aerogel, ρ_{Gel} is the density of the aerogel, and ρ_{CNC} is the density of CNCs which is assumed to be 1.59 g cm⁻³ [44].

Nitrogen sorption isotherms

Specific surface area and pore size of the CNC aerogels were obtained by Brunauer–Emmett–Teller (BET) analysis of the nitrogen sorption isotherms collected with an Autosorb[®] iQ (Quantachrome, Boynton Beach, USA). The aerogel samples (100–200 mg) were first degassed and then kept under nitrogen gas at 100 °C for 7 days prior to obtaining the nitrogen sorption isotherms. CNCs are hydrophilic, and CNC aerogels have large specific surface areas available to bind water tightly; as such, this extensive drying was necessary to obtain reproducible results to not interfere with the nitrogen gas probing. Furthermore, to show that the drying process had removed all water, an additional adsorption/desorption curve was performed for one sample of each aerogel type to ensure that the nitrogen sorption isotherms were nearly identical and that there was no gap between the adsorption and desorption curves at zero relative pressure. The nitrogen sorption isotherms were obtained at –196 °C, and specific surface area and pore distributions were calculated using density functional theory (DFT) [45]. DFT analysis is built into the Quantachrome software and is more reliable in this case than Barrett–Joyner–Halenda (BJH) analysis that assumes that N₂ condensation forms a half sphere meniscus, which is unlikely for our non-spherical pores and particularly the small mesopores. Only isotherms that showed no retention of water was used to acquire specific surface area and pore size distribution.

Scanning electron microscopy (SEM) imaging

Aerogel samples were submerged into liquid nitrogen and fractured to gain an exposed cross section for SEM analysis. Samples were mounted on a 1" diameter stainless steel stub with nickel paint. Nickel paint was used to coat the sides of the aerogel to create a connection to the sample stage to avoid charge buildup. Aerogels were sputter-coated with a 5-nm-thick platinum coating and imaged in a JEOL 7000F SEM (JEOL, Tokyo, Japan) and a Magellan 400 XHR FE-SEM (FEI, Oregon, USA). All aerogel images were taken at a working distance between 4–6 mm and at an acceleration voltage of 2 kV.

X-ray micro-computed tomography (μ CT)

Aerogel samples were stained with an osmium tetroxide/thiocarbohydrazide staining protocol [46] in order to increase contrast for μ CT analysis. To coat cryo-templated aerogels, the aerogels were submerged into a 1 wt% osmium tetroxide solution for 1 h. Next, the aerogel was rinsed with purified water until no osmium tetroxide remained. After every rinse, a single drop of 0.5 wt% thiocarbohydrazide (TCH) solution was dropped into the rinsing water. If a black or brown color change occurred, it would indicate remaining osmium tetroxide and an additional rinse would be required. After the aerogel was rinsed, it was submerged into 0.5 wt% TCH solution for 10 min. The aerogel was rinsed again using the same method and criteria, but with a drop of 1 wt% osmium tetroxide to test the rinsing water. The aerogel was then submerged into an additional 1 wt% solution of osmium tetroxide for 10 min. The aerogel was rinsed with purified water and submerged into anhydrous ethanol, then subjected to CPD. For PGX aerogels, the aerogel was placed in a parafilm-sealed petri dish, with four droplets of 1 wt% osmium tetroxide for 4 h. The osmium tetroxide solution caused a light chemical vapor deposition of osmium tetroxide on the PGX aerogel surface. Both samples were mounted on a 2.5" diameter brass stub and analyzed with a SkyScan 1172: High Resolution Desk-Top Micro-CT (Bruker, USA), with a 40 kV X-ray beam, with no filter, 7 μ m pixel size, and a 0.3° rotation step.

X-ray diffraction (XRD)

The degree of crystallinity of CNC samples was measured by XRD using a Bruker D8 Davinci diffractometer (Bruker, Massachusetts, USA). Samples were prepared by taking CNC aerogels and compressing them to a thin uniform puck. Measurements were taken with a cobalt-sealed tube source emitting a wavelength of 1.79026 Å, at an acceleration voltage of 35 kV, and a probe current of 45 mA with a parallel Gobel Mirror, Vantec 500 area detector, 0.5 mm short collimator covering a 2θ range of 8°–45°, and a 0.5-mm slit opening. Silicon wafer blanks were used to subtract background noise from all XRD diffraction patterns. Diffraction patterns were analyzed using Rietveld refinement as shown in the literature [43]. The amorphous phase was modeled

using a pseudo-Voigt function with a fixed amorphous peak at 24.1° for all CNC samples. We take the experimental and fitting error in these measurements to be ca. 5% as reported previously [43].

X-ray photoelectron spectroscopy (XPS)

XPS was used to compare the amount of hydrazone cross-linking between PGX and cryo-templated CNC aerogels. Samples for XPS were prepared by compressing aerogels into a thin uniform puck. Samples were measured using a Physical Electronics (PHI) Quantera II spectrometer (Chanhassen, USA) using a Al K α X-ray source (1486.7 eV) operating at 50 W and 15 kV with a system pressure not allowed to exceed 1.0×10^{-9} Torr and an operating pressure of 2.0×10^{-8} Torr. Pass energy of 280 eV was used to collect the survey spectra, and a 55 eV was used to collect high-resolution nitrogen spectra. All spectra were collected at a takeoff angle of 45°, and a dual beam charge compensation system was used for the neutralization of all samples. Data were processed using PHI MultiPak Version 9.4.0.7 software. We consider the error in the spectra to be ca. 5%.

Compression testing

Mechanical stress–strain curves in compression were measured for both PGX and cryo-templated CNC aerogels using a Mach-1 Mechanical Testing System (Biomomentum, Laval, Canada). For cryo-templated aerogels, a 15-mm-diameter shell vial was used as a mold. The vial was filled with 1 mL of the mixed CNC suspension and then processed using the cryo-templating method outlined above. PGX aerogel samples were prepared by using a custom stainless steel cylindrical sample cutter to cut samples out of the bulk aerogel at random locations. A razor was used to cut the cylinder to the appropriate height to be approximately the same height as the cryo-templated aerogel samples. All aerogels ranged between 8–10 mm in diameter and 7–10 mm in height. All samples were compressed to 90% of their maximum height at a compression speed of 0.1 mm/s under dry ambient conditions. Three separate samples for each type of aerogel were tested, and error intervals reported are standard deviations.

Results and discussion

Characterization of cross-linkable CNCs

In order to fabricate chemically cross-linked CNC aerogels, sulfuric acid-hydrolyzed CNCs were first surface-modified with orthogonal functional groups, namely aldehyde and hydrazide groups leading to CHO-CNCs and NH₂NH-CNCs, respectively. These modified CNCs form hydrazone bonds immediately when in contact [25]. All surface modifications employed straightforward water-based chemistries wherein CNCs remain well dispersed, which we believe is necessary to promote uniform functionalization. The reactions gave a similar density of both aldehyde and hydrazide groups on the CNC surface, as shown in Table 1. While it is important to have sufficient cross-link points on the CNCs to facilitate “locking in” of the aerogel network structure, it is likely that due to geometric constraints (and the inflexibility of CNCs) that not all aldehyde groups on CHO-CNCs react with all hydrazide groups on NH₂NH-CNCs. Both PGX and cryo-templated aerogels were produced from the same CHO-CNC and NH₂NH-CNC batches and were characterized extensively prior to use.

Table 1 shows the surface group content (measured through conductometric titration), apparent particle size by DLS, zeta potential, and degree of crystallinity from XRD for all CNCs produced.

All modified CNCs remained colloiddally stable by eye, despite the decrease in anionic sulfate half-ester content after aldehyde functionalization (Table 1). CHO-CNCs had the lowest absolute zeta potential resulting in some aggregation in suspension [47] as evidenced by DLS. TEMPO oxidation of sulfated CNCs did not lead to changes in the sulfate half-ester content, and COOH-CNCs had a similar zeta potential to the neat CNCs; however, carbodiimide

coupling to produce NH₂NH-CNCs from COOH-CNCs removes some charge groups leading to a decrease in the absolute zeta potential. COOH-CNCs and NH₂NH-CNCs are slightly larger than neat CNCs, potentially due to some peeling of surface cellulose chains during oxidation which can give partially “hairy” structures [48]. In all cases, CNCs remained anionic and nano-sized and the surface modification reactions did not compromise their high degree of crystallinity.

Processing of CNC aerogels

Cross-linked CNC aerogels were produced by critical point drying cryo-templated alco-gels and by PGX processing CNC ethanol–water slurries. While the two processes seem similar in terms of the solvents used, there are some key differences. Namely, the solvent exchange and removal of water happen in a batch-wise manner over long periods of time in the cryo-templating CPD process, whereas in the PGX process the particle slurry is continuously pumped into a mixture of ethanol and supercritical CO₂ leading to a single-phase regime and instant solvent exchange, thereby causing precipitation and formation of the aerogel-like structure. In the PGX process, gel network formation, precipitation, and dehydration all occur in fractions of seconds using the coaxial nozzle to mix the aqueous slurry with the CO₂ and ethanol mixture under a highly turbulent regime while feeding into a pressurized collection vessel (Fig. 1). It is important to note that the PGX feed process does not result in spraying/droplet formation because the interfacial tension vanishes as the miscible fluids rapidly form a single phase [32, 35]. As a result, the PGX process preserved preexisting non-agglomerated structures from the wet state to the dried state, in contrast to techniques that include evaporation of droplets such as spray drying, or

Table 1 Surface functional group content, apparent particle size, zeta potential, and degree of crystallinity for neat and surface-modified CNCs used in the preparation of cross-linked aerogels

Type of CNC	Sulfate half-ester content (mmol g ⁻¹)	Aldehyde content (mmol g ⁻¹)	Carboxylic acid content (mmol g ⁻¹)	Hydrazide content (mmol g ⁻¹)	Apparent particle size (nm)	Zeta potential (mV)	Crystallinity index (%)
Neat CNC	0.212 ± 0.002	–	–	–	90 ± 1	– 40 ± 3	97
CHO-CNC	0.122 ± 0.003	1.80 ± 0.01	–	–	140.1 ± 0.6	– 17.2 ± 0.2	89
COOH-CNC	0.210 ± 0.002	–	1.20 ± 0.03	–	90.4 ± 0.6	– 40 ± 5	91
NH ₂ NH-CNC	0.211 ± 0.004	–	0.60 ± 0.03	0.60 ± 0.03	98.2 ± 0.8	– 30 ± 3	87

freezing steps, which condense the solutes and greatly alter any preexisting structures.

In the PGX process, at the flowrates chosen in this study, the injection of the CNC slurry concurrently with the PGX fluid, which is a mixture of CO₂ and ethanol at 40 °C and 100 bar, forms a so-called gas-expanded liquid with unique properties [41, 49, 50], leading to a completely miscible ternary system, which has been described extensively before [51–55]. Thus, injecting the CNC ethanol–water slurry and PGX fluid concurrently by means of a coaxial nozzle causes the aqueous feed stream to immediately disperse and the fluid phases to dissolve in each other. More specifically, water dissolves into the co-injected gas-expanded “CO₂ plus ethanol” fluid thereby leading to solvent exchange and CNCs suspended in PGX fluid. The CNC network is captured in the collection vessel and residual water is removed with excess PGX fluid once all CNC slurry is injected, while still operating in the single-phase region.

Using PGX processing with cross-linkable CNCs, we were able to obtain highly porous structures through a one-pot continuous process which (depending on PGX setup, sample size, and CV volume) takes from 3 to less than 8 h total per batch. On the other hand, in the cryo-templating method, each solvent is sequentially removed in a diffusion controlled process taking up to 5 days, until the gel is subjected to the drying process (which took another 2 h for small samples) using supercritical CO₂.

Another difference between the two processes is that colloidal stability of small cross-linked CNC clusters is a prerequisite to obtain uniform and porous aerogels by cryo-templating and CPD [25], whereas the “feed” in the PGX process was a loosely gelled slurry of CNCs in ethanol and water. We found that it was beneficial for the specific PGX setup used in this study for CNCs to be suspended in 90% ethanol (despite ethanol being a poor dispersion media for CNCs) because it reduced the initial amount of water that needed to be removed. However, it required the slurry to be sheared prior to being pumped into the PGX system. Otherwise, when a fully aqueous slurry of CNCs was introduced to the PGX system, an aggregated jelly-like material formed inside of the inlet which prevented the system from properly feeding material into the collection vessel. Importantly, high shear mixing after suspending CNCs in ethanol was required to achieve slurry viscosities that were compatible with the PGX process.

For example, the un-sheared CNC slurry had a viscosity of 35 ± 0.2 mPa.s and contained aggregated/gelled material. High shear mixing was able to reduce the slurry viscosity to 1 ± 0.2 mPa.s, which was more easily processed in the PGX system. Furthermore, with less than 90% ethanol in the slurry it was difficult to obtain fully dried CNC materials with the PGX protocol used in this study.

There are three separate “mechanisms” that ultimately affect the aerogel morphology in the PGX process because they change how the CNCs are precipitated and dehydrated. These mechanisms all occur more or less simultaneously upon feeding the CNC ethanol–water slurry into the high-pressure collection vessel. First, the CNC ethanol–water slurry is rapidly mixed in a coaxial nozzle with the gas-expanded drying fluid, consisting of CO₂ and ethanol, which has low viscosity and full miscibility with the slurry. During that mixing step, supercritical CO₂ acts as an intermediate between water and ethanol thereby leading to miscibility and an improved mass transport with low or no interfacial tension. This allows faster and more homogeneous dehydration without collapsing the porous structures due to capillary forces. In this work, all PGX aerogels were produced using the same coaxial nozzle. However, additional morphological control is anticipated through altering the orifice size and design of the nozzle. Second, the anti-solvent effect of ethanol further precipitates the CNCs out of its original ethanol–water solution. Third, the supercritical CO₂ stream carries the ethanol and water outside of the vessel, while the CNCs remain in the vessel. When the system is returned to ambient pressure, the supercritical CO₂ becomes a gas and leaves behind the dried networked CNC structures characterized in detail below.

Macroscopic comparison of CNC aerogels

Cryo-templated and PGX aerogels had different macroscopic appearances, as shown in Fig. 2. Both aerogels were lightweight and opaque, consistent with previously reported CNC aerogels [12]. Cryo-templated aerogels were sponge-like, flexible, and mechanically robust when compressed by hand (Fig. 2a), whereas the PGX aerogels had a fluffier appearance and fragile structure (Fig. 2b). As a control, we attempted to CPD the PGX feed material (i.e., the CNC ethanol–water slurry) without the freezing

or solvent exchange steps; a dense material (1.5 ± 0.06 g/mL) with a porosity of 2–8% was obtained which was not considered an aerogel and further characterization was curtailed. In water, both types of aerogels remained intact; however, cryo-templated aerogels maintained their form (Fig. 2c), while the PGX aerogel volume decreased (Fig. 2d). These physical differences can be attributed to the differences in their microstructure, as discussed further below.

Microstructural analysis and comparison of CNC aerogels

SEM imaging was performed on both types of CNC aerogels to investigate the internal aerogel morphology (Fig. 3). Cryo-templated aerogels had a bimodal pore size distribution resulting from the stacking of mesoporous CNC sheets separated by macropores (Fig. 3a), as reported previously [25]. The CNC sheets were random in shape and size due to ice-crystal growth during freezing. Figure 3b and 3c shows higher-magnification images of a CNC sheet with uniformly distributed and similarly nano-sized mesopores, which result from CNCs cross-linking in a non-parallel manner. Macropore sizes vary widely from ca. 10 to 950 μm , as determined through image

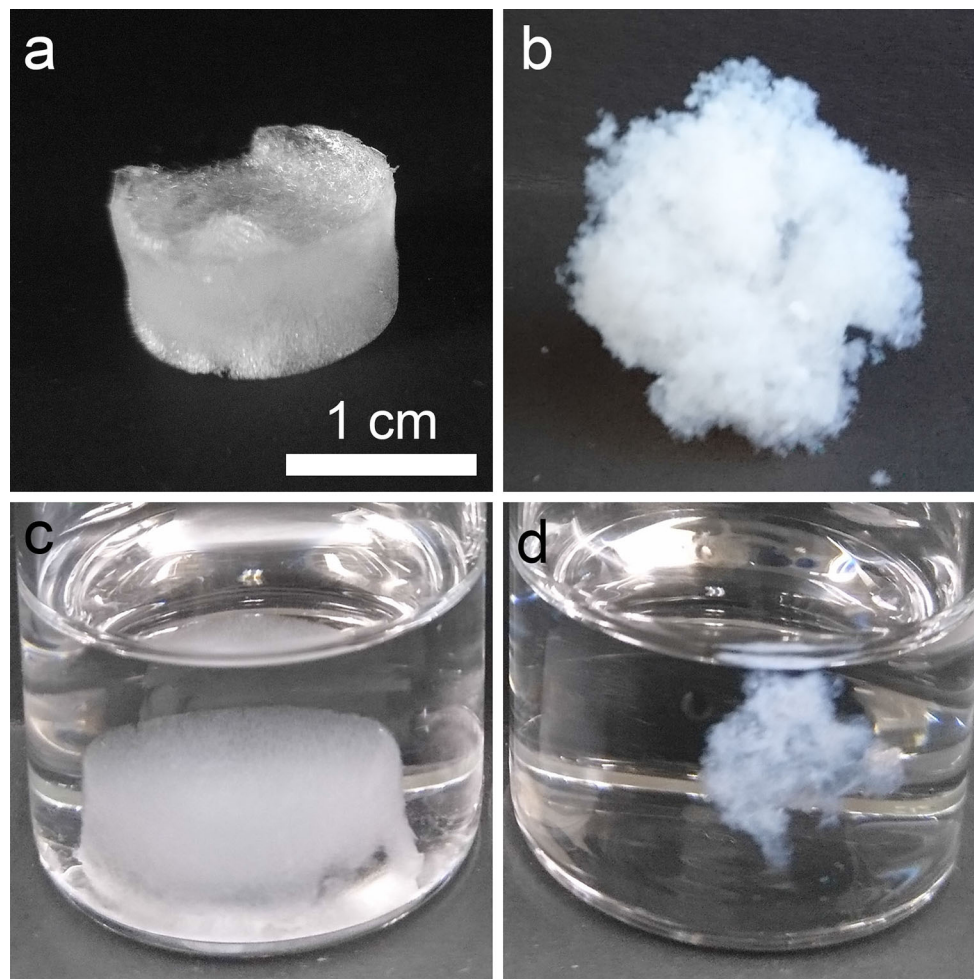


Figure 2 Comparison of the macroscopic appearance of cryo-templated and PGX CNC aerogels in dry and wet states, the scale bar in (a) applies to all images. **a** A dry cryo-templated aerogel, **b** a dry PGX aerogel, **c** a cryo-templated aerogel submerged in water,

and **d** a PGX aerogel submerged in water. The cryo-templated aerogel retained its shape in water, whereas the PGX aerogel shrank; neither aerogel redispersed due to chemical cross-linking.

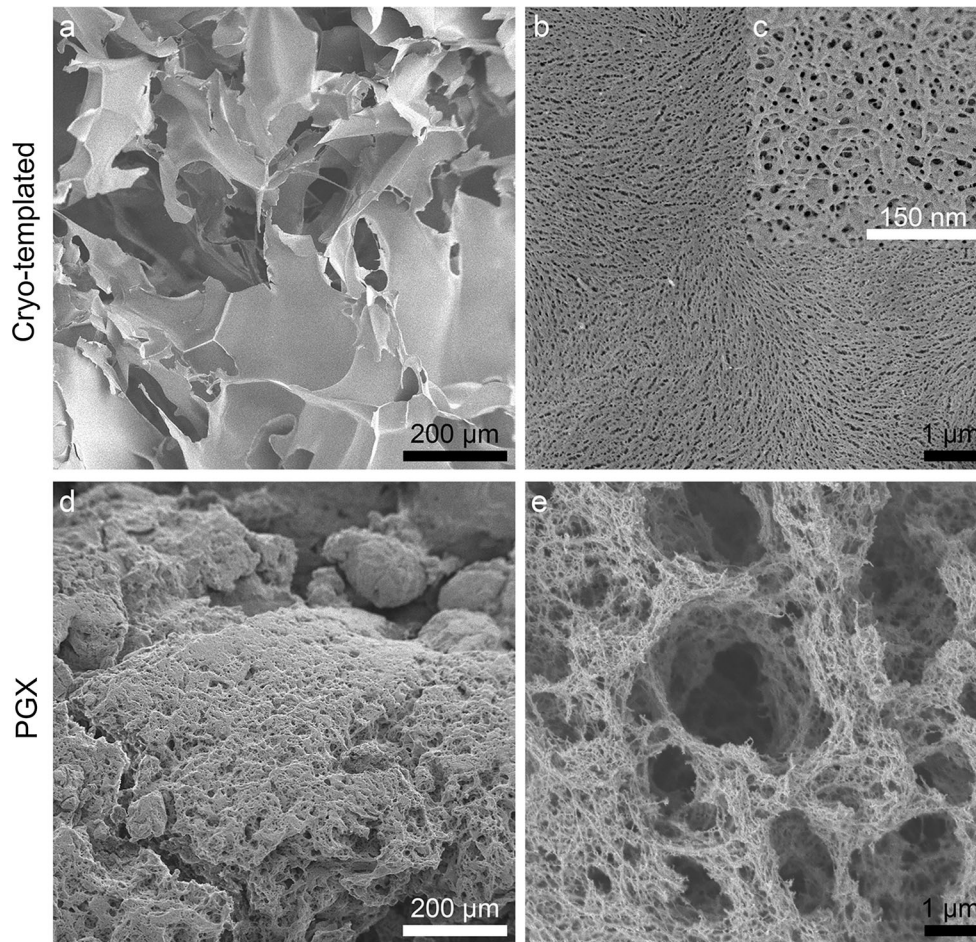


Figure 3 SEM images of the (a–c) cryo-templated and (d–e) PGX aerogels. **a** CNC sheet morphology of cryo-templated aerogels separated by large ice-templated macropores, **b** surface of the CNC sheets, revealing the large distribution of mesopores, **c** a

higher magnification of a CNC sheet with well-defined mesopores, **d** the porous mound-like morphology of the PGX aerogels, and **e** the expanded and fibrillar microstructure of the PGX aerogel mounds with a large range of mesopores and small macropores.

line analysis using ImageJ software and measuring > 100 macropores.

On the other hand, PGX aerogels had a mound-like morphology (Fig. 3d), likely due to the aggregation induced when CNCs were mixed at high shear rates and suspended in the ethanol–water mixture prior to PGX processing. However, the mounds themselves were much more fibrillar and porous compared to the CNC sheets, as shown in Fig. 3e. We see this mound-like morphology throughout the sample and believe it represents the structure fed into the PGX reactor and is not due to the freeze fracturing sample preparation used for all aerogels prior to SEM imaging; the PGX samples were easy to fracture which we hope means minimal changes to the original morphology. The macropores for PGX aerogels were much smaller than cryo-templated aerogels at

approximately 1–4 μm . We infer that CNCs further cross-link while being pumped and fed through the nozzle, where the mixture is intensely mixed with the CO_2 -expanded ethanol leading to dilution of the CNC slurry. During the feed step of PGX processing, the CO_2 expanded fluid is completely miscible with the aqueous CNC slurry which minimizes any further agglomeration due to capillary forces, so that the CNCs stay separated and “expanded” thereby producing a large distribution of mesopores and fairly small macropores.

We believe that the PGX aerogels shrink in water because they are less dense and their fibrillar nature is more flexible than the cryo-templated aerogels. The reduction in size of the structure is attributed to fibrils being drawn together through capillary forces. As water wets the PGX aerogel, the morphology is not

strong enough to resist forces pulling the fibrils together, causing the overall PGX material to shrink. This contrasts cryo-templated aerogels that can retain their shape in water (and other solvents) because the cross-linked CNC sheets are not flexible enough to bend/collapse when wetted.

Both types of aerogels were also evaluated using X-ray micro-computed tomography; the 3D reconstructions are shown in Fig. 4 and complement the SEM images (Fig. 3). The macropores of cryo-templated aerogels that separate the CNC sheets are observable in Fig. 4a, where the white represents the CNC sheets and the black vacancies represent the macropores. Orthogonal slices indicate that the entire pore morphology is interconnected in the cryo-templated aerogel. In contrast, the PGX aerogel has almost no visible macropores; instead, a faded gray appearance with denser white regions is seen (Fig. 4b). The faded appearance is due to a lack of macropores greater than 7 μm (i.e., the resolution limit of μCT with the chosen imaging parameters),

which agrees with Fig. 3d and 3e. This highlights that the two processing methods have given aerogels with completely different pore structures despite both being fairly uniform, albeit in a different way.

The white features in Fig. 4 are aggregated regions of cross-linked CNCs with densities similar to the sheets observed in cryo-templated aerogels. These regions were likely formed before or during the feeding of the CNC ethanol–water slurry into the PGX vessel and may have contained trapped water that could not be fully dehydrated during the process. Additionally, the different microstructure and density of the aggregated regions likely affect staining with OsO_4 , where more uptake of stain would contribute to the change in contrast noted in the μCT images. SEM images of these dense regions are shown in Fig. 4c which suggests that these aggregates are more condensed than the fluffy mounds surrounding them and do not contain macropores. Figure 4d shows a higher magnification of the aggregated region, which reveals that there are still

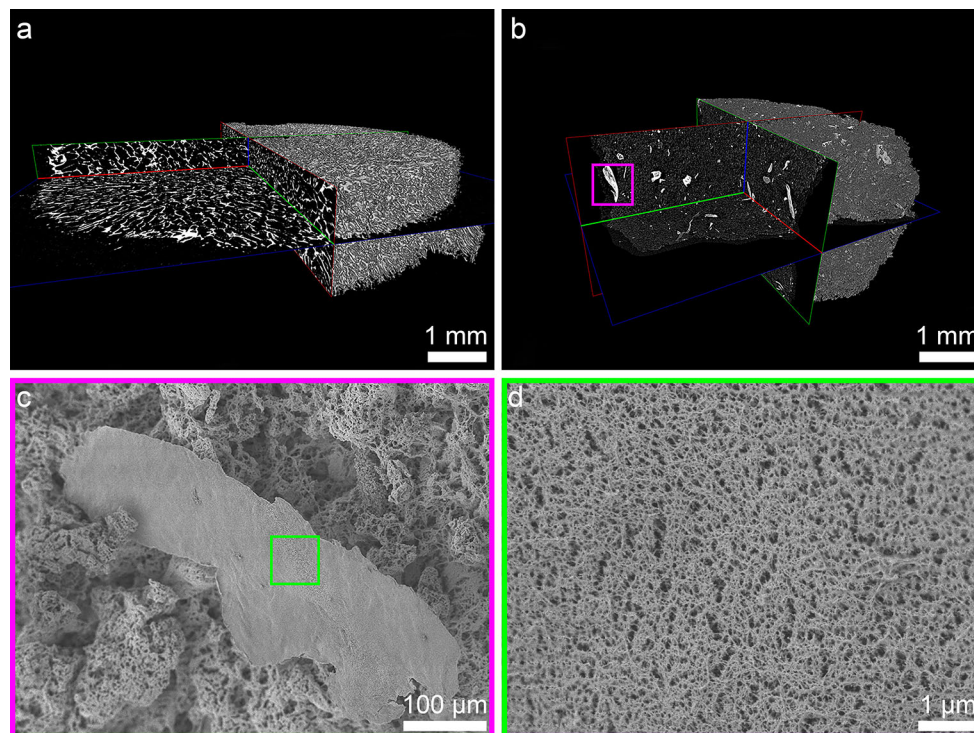


Figure 4 Micro-computed tomography 3D reconstructions with orthogonal slices of **a** cryo-templated aerogels and **b** PGX aerogels. The cryo-templated aerogels have an interconnected macroporous structure and a large distribution of macropores, whereas PGX aerogels lack macropores greater than 7 μm (which appear as faded gray areas) and have some aggregated regions

(which appear white, one example of an aggregate is highlighted in the purple box). SEM of the **c** purple- and **d** green-boxed regions is used to show the microstructure of the white aggregated regions in **(b)**. Aggregates do not have visible macropores but do have mesopores and are more like the dense CNC sheets in cryo-templated aerogels.

mesopores between individual CNCs, similar to the high-magnification images of the sheets in the cryo-templated aerogels. While outside of the scope of this current work, it is likely that the PGX process could be tailored to have more or less of these dense regions in order to control the porosity and mechanical properties of the aerogels.

To *quantify* the microstructure and morphology of CNC aerogels, density and porosity were determined, BET and DFT analysis of nitrogen sorption isotherms was performed, and XRD was used to ensure that no degradation of the cellulose crystal structure occurred during the aerogel processing. Table 2 presents these values, where cryo-templated aerogels were in line with previously reported work [25] and PGX aerogels had almost double the specific surface area, half the density, and were therefore slightly more porous. These values agree qualitatively with the SEM and μ CT images (Fig. 3 and Fig. 4). The much higher specific surface area in PGX aerogels results from the PGX process and the avoidance of freezing steps. It should be noted that both specific surface area values in Table 2 remain below the theoretical limit for CNCs aerogels. (We take the theoretical limit for CNC aerogels as the specific surface area of a completely isolated CNC—for CNCs produced by sulfuric acid hydrolysis; this value is ca. $512 \text{ m}^2 \text{ g}^{-1}$ assuming a length of 130 nm, a width of 5 nm [25], and a density of 1.59 g cm^{-3} [44].)

The crystallinity values for both types of aerogels were within experimental error (ca. 5%) based on XRD analysis, showing that CNC crystallinity had been maintained during aerogel processing (Table 2). While the best method to measure CNC crystallinity remains debated in the literature [43], we believe XRD has the resolution and accuracy to deduce useful relative values. For the PGX process there was some concern that the supercritical conditions could cause the cellulose degree of polymerization to decrease; however, this was not the case and both

types of aerogels had crystallinities well within accepted values [43] and similar to the starting neat and modified CNCs (Table 1).

In addition to the specific surface area, BET analysis of nitrogen sorption isotherms combined with DFT processing provides further information about the pore size and distribution for pores below 50 nm (Fig. 5). Cryo-templated aerogels had two well-defined peaks indicating pore diameters of 3.9 nm and 11.1 nm (Fig. 5a), similar to values reported previously [25, 56]. This is further supported by the mesopore sizes observed in Fig. 3c. (And then the large macropores that tend to be over $10 \mu\text{m}$ make up the rest of the aerogel porosity and are not measurable by nitrogen sorption.) Figure 5a also shows a broad peak from 13 to 36 nm that may be due to the random CNC orientation during the cryo-templating process. As CNCs are excluded from the growing ice crystals and pushed together, rigid aggregates form until they are fully condensed into CNC sheets and depending on the exact orientation of CNCs as they cross-link, a range of pore shapes and sizes is expected.

Interestingly, DFT analysis of the PGX aerogel nitrogen sorption isotherms also showed some pore sizes that are very similar to the cryo-templated aerogels, namely 3.5 and 11.1 nm (Fig. 5b). This may suggest that when CNCs are being pushed together, there are preferred conformations (e.g., an orientation that minimizes electrostatic repulsion or maximizes van der Waals attraction). In the PGX aerogels, distinct peaks at 1.4, 6.8, and 17.9 nm were also observed showing that there are more sizes of mesopores present than in cryo-templated aerogels. Finally, the increasing slope between 45 and 50 nm for PGX aerogels further reinforces this, as this shows that pore size is also distributed in the low end of the macropore range, in agreement with Fig. 3e. These data indicate that PGX aerogels have a large range of pore sizes from mesopores to the lower end of

Table 2 Specific surface area, density, porosity (calculated using Eq. 2), and degree of crystallinity of cryo-templated and PGX aerogels

Type of CNC aerogel	Specific surface area ($\text{m}^2 \text{ g}^{-1}$)	Density (mg cm^{-3})	Porosity (%)	Crystallinity index (%)
Cryo-templated	190 ± 20	10.0 ± 0.8	99.3	87
PGX	320 ± 10	6 ± 1	99.6	91

Specific surface area and density values are shown here with their respective standard deviations

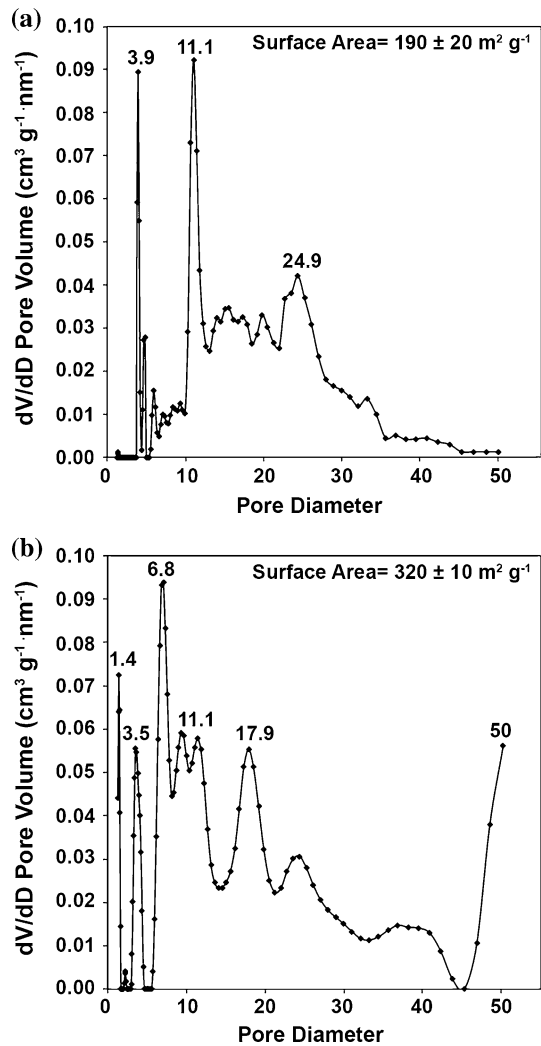


Figure 5 Analysis of nitrogen sorption isotherms showing the pore size distribution of **a** cryo-templated aerogels and **b** PGX aerogels. Specific surface area values are shown in insets, and pore dimensions in nm are annotated above their respective peak (dV/dD is the derivative of the pore volume taken with respect to the pore diameter).

macropores, in contrast to the cryo-templated aerogel's primarily bimodal pore size distribution.

Comparison of hydrazone cross-linking in aerogels

XPS was used to quantify the number of hydrazone bonds present within both types of aerogels. While XPS can present challenges with cellulose materials that are well known to be susceptible to hydrocarbon contamination [43, 57], high-resolution nitrogen peak deconvolution can help us better understand the aerogels prepared in this work. Table 3 shows the

atomic composition of the different types of nitrogen bonding for cryo-templated and PGX-processed aerogels. Specifically, peaks with bond energy = 400.13 eV correspond to amine bonds (N-H₂) and hydrazine bonds (N-N) and peaks with bond energy = 401.09 eV correspond to hydrazone bonds (C = N). With more cross-linking the amine/hydrazine peak decreases and the hydrazone peak increases; Table 3 shows that overall, cryo-templated aerogels have more hydrazone bonds (i.e., are more cross-linked) than PGX aerogels.

Enhanced cross-linking in cryo-templated CNC aerogels is likely related to the nature of the production process, which is relatively slow, and forces CNCs together by excluding them from the growing ice front. The force during this process is sufficient to overcome short-range repulsive forces that normally keep CNCs apart; this maximizes the potential for cross-linking. On the other hand, during PGX drying, CNCs are never forced together to this extent—they are colloiddally unstable in ethanol because ethanol is a poor dispersant [58] and this combined with the high shear mixing prior to pumping CNCs into the PGX vessel increases the likelihood of CNCs coming into contact and cross-linking but not to the same extent as freezing. Although cryo-templated aerogels and PGX aerogels differ in their morphology and cross-link density, they remain intact in water, which was the main goal of producing covalently cross-linked CNC aerogels.

Aerogel mechanical properties

Lastly, the compressive strength of CNC aerogels was measured by mechanical compression testing. Cryo-templated aerogels were found to be stiffer than PGX aerogels, as shown in Fig. 6. At 90% compression, the cryo-templated aerogels displayed a compressive stress of 94 ± 2 kPa, compared to PGX

Table 3 High-resolution nitrogen XPS analysis showing the atomic composition of the different types of nitrogen bonding for cryo-templated and PGX-processed aerogels

Type of aerogel	Atomic composition (%)	
	Amine/hydrazine	Hydrazone
Cryo-templated	55.0	45.0
PGX	75.4	24.6

aerogels, which displayed a compressive stress of 7 ± 2 kPa. This is likely related to the dense CNC sheets within the cryo-templated aerogels as well as the less porous structure and the higher cross-link density. As the aerogel is being compressed, the sheets begin to bend and stack until all space provided by the macropores is gone and this compressed structure offers enhanced strength. Cryo-templated aerogels have also been shown to have good shape recovery properties in both air and water [25].

Oppositely, PGX aerogels are more easily compressed which is attributed to them having a more open, porous structure with fewer condensed/cross-linked regions to provide reinforcement. This concurs with the shrinking behavior of PGX aerogels in water, where capillary forces are sufficient to compress the internal structure, which is not the case for the stronger cryo-templated aerogels. It is also interesting to note that the consistency and reproducibility of the PGX-produced aerogels was highlighted through the mechanical testing results: Samples for compression were randomly cut from the large bulk aerogel yet consistent mechanical properties were measured (as seen from the small standard deviation of ± 2 kPa over 3 samples).

The argument that cross-link density affects the compressive behavior of CNC aerogels (in addition to pore morphology) is supported by previous work in our group where cryo-templated CNC aerogels produced from 1 wt% CNC suspensions (with

hydrazone cross-linking) had a compressive stress of only 18 kPa at 90% compression [25]. This is five times lower than the values seen in this work, and the main difference is the density of the surface functionalization on CNCs (i.e., the number of aldehyde and hydrazide groups available for cross-linking). In both works, hydrazide groups are the “limiting” cross-linking group (Table 1) and we have roughly five times more hydrazide groups here than in our previous report [25]. While it seems difficult to visualize more than a few CNCs cross-linking in a given plane based on their size and rigidity, one possibility is that sheets can stack more easily (or more cross-linking in three dimensions) with more cross-link sites leading to thicker CNC sheets, which would in turn yield an aerogel more resistant to compression. We note that the differences in mechanical properties between cryo-templated and PGX aerogels are likely a combination of morphology, density, porosity, and number of cross-links. We investigated normalizing the stress data in Fig. 6 by the mass of the aerogel sample, the density, the specific surface area, and the ratio of hydrazone bonds (from Table 3 related to total amount of cross-linking); the two series came closer to each other but did not superimpose based on any single parameter alone (data not shown) which implies a compound effect.

Conclusions

Through this work, we have shown the impact that aerogel processing methods can have on CNC aerogel morphology and performance. Despite both the cryo-templated and PGX process using the same cross-linkable CNCs as the starting material and using water, ethanol, and supercritical CO₂ as solvents, two different aerogels were produced. The PGX technology produced a more expanded, fibrillar, and porous CNC aerogel with a greater specific surface area and a wider range of smaller pore sizes compared to cryo-templated aerogels. PGX aerogels had lower compressive strength and also shrank when submerged in water, whereas cryo-templated aerogels maintained their shape. The pore size distribution for both types of aerogels implied that there are some preferred geometry/spacings when CNCs come together to cross-link and well-defined mesopores are achievable regardless of the processing

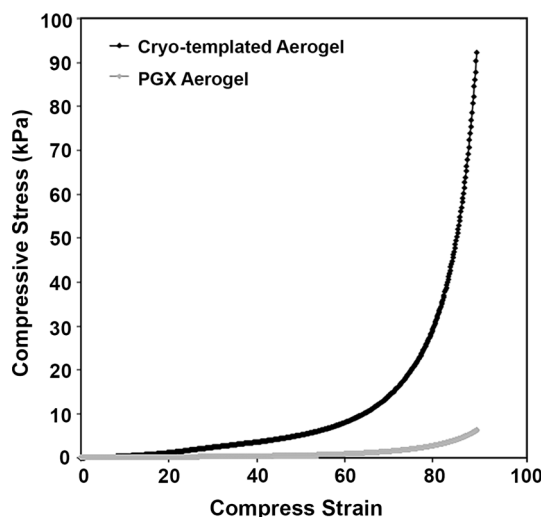


Figure 6 Representative compressive stress–strain curves for cryo-templated (black) and PGX (gray) aerogels from 0 to 90% strain. It can be seen that the cryo-templated aerogel is more resistant to compression than the PGX aerogel.

method. Pore size, the ratio of meso- to macropores and cross-link density affected aerogel mechanical properties. With consistent compressive strength, specific surface area, and density measured across multiple samples, it is evident that the PGX process can produce uniform and reproducible CNC aerogels. We believe that the morphology of cross-linked CNC aerogels can be tuned through the processing methods used and that PGX drying is a more industrially feasible route to prepare aerogels that may find application as sound and thermal insulation, drug delivery, gas separation/capture, and template materials.

Acknowledgements

The authors would like to thank Ceapro Inc. for their cooperation, useful discussions, and access to PGX equipment. Funding is from the Natural Sciences and Engineering Research Council of Canada (NSERC) Discovery Grants RGPIN 402329 and RGPIN 588778. NSERC Engage Grant 492456-15 with Ceapro Inc., Alberta Innovates project ABI-15-001, and support from the Faculty of Engineering at McMaster University are gratefully acknowledged. We also thank N. Kudeba and L. Delgado at Ceapro for help with the production of PGX samples. We thank Professors T. Hoare, R. Pelton, A. Guarne, the Canadian Center for Electron Microscopy (CCEM), the McMaster Automotive Resource Center (MARC), McMaster Biointerfaces Institute, and the University of Waterloo for shared equipment. A. Kacheff, K.A. Johnson, I. Shahid, J. Tedesco, M. Reid, V. Jarvis, N. Belsito, T. Stimpson, and Dr. D. Covelli are gratefully acknowledged for training, sample analysis, and expertise. D. O. would like to extend a special thanks to X. Yang, for his pioneering work on CNC aerogels and guidance throughout this work.

References

- [1] Du A, Zhou B, Zhang Z, Shen J (2013) A special material or a new state of matter: a review and reconsideration of the aerogel. *Materials (Basel)* 6:941–968. <https://doi.org/10.3390/ma6030941>
- [2] Hrubesh LW (1998) Aerogel applications. *J Non Cryst Solids* 225:335–342. [https://doi.org/10.1016/S0022-3093\(98\)00135-5](https://doi.org/10.1016/S0022-3093(98)00135-5)
- [3] Tao Y, Endo M, Kaneko K (2008) A review of synthesis and nanopore structures of organic polymer aerogels and carbon aerogels. *Recent Patents Chem Eng* 1:192–200. <https://doi.org/10.2174/1874478810801030192>
- [4] Zou J, Liu J, Karakoti AS et al (2010) Ultralight multiwalled carbon nanotube aerogel. *ACS Nano* 4:7293–7302
- [5] Gui X, Wei J, Wang K et al (2010) Carbon nanotube sponges. *Adv Mater* 22:617–621. <https://doi.org/10.1002/adma.200902986>
- [6] Zhu C, Han TY, Duoss EB et al (2015) Highly compressible 3D periodic graphene aerogel microlattices. *Nat Commun* 6:1–8. <https://doi.org/10.1038/ncomms7962>
- [7] Bandi S, Bell M, Schiraldi DA (2005) Temperature-responsive clay aerogel—polymer composites. *Macromolecules* 38:9216–9220
- [8] Sehaqui H, Morimune S, Nishino T, Berglund LA (2012) Stretchable and strong cellulose nanopaper structures based on polymer-coated nano fiber networks: an alternative to nonwoven porous membranes from electrospinning. *Biomacromol* 13:3661–3667
- [9] Sehaqui H, Zhou Q, Berglund LA (2011) High-porosity aerogels of high specific surface area prepared from nanofibrillated cellulose (NFC). *Compos Sci Technol* 71:1593–1599. <https://doi.org/10.1016/j.compscitech.2011.07.003>
- [10] Klemm D, Heublein B, Fink H, Bohn A (2005) Polymer science cellulose: fascinating biopolymer and sustainable raw material. *Angew Chemie Int Ed* 44:3358–3393. <https://doi.org/10.1002/anie.200460587>
- [11] Nechyporchuk O, Belgacem MN, Bras J (2016) Production of cellulose nanofibrils: a review of recent advances. *Ind Crop Prod* 93:2–25. <https://doi.org/10.1016/j.indcrop.2016.02.016>
- [12] De France KJ, Hoare T, Cranston ED (2017) Review of hydrogels and aerogels containing nanocellulose. *Chem Mater* 29:4609–4631. <https://doi.org/10.1021/acs.chemmater.7b00531>
- [13] Beck-Candanedo S, Roman M, Gray DG (2005) Effect of reaction conditions on the properties and behavior of wood cellulose nanocrystal suspensions. *Biomacromol* 6:1048–1054. <https://doi.org/10.1021/bm049300p>
- [14] Roman M (2015) Toxicity of cellulose nanocrystals: a review. *Ind Biotechnol* 11:25–33. <https://doi.org/10.1089/ind.2014.0024>
- [15] Eyley S, Thielemans W (2014) Surface modification of cellulose nanocrystals. *Nanoscale* 6:7764–7779. <https://doi.org/10.1039/C4NR01756K>
- [16] Habibi Y, Lucia LA, Rojas OJ (2010) Cellulose nanocrystals: chemistry, self-assembly, and applications. *Chem Rev* 110:3479–3500. <https://doi.org/10.1021/cr900339w>

- [17] Leung ACW, Hrapovic S, Lam E et al (2011) Characteristics and properties of carboxylated cellulose nanocrystals prepared from a novel one-step procedure. *Small* 7:302–305. <https://doi.org/10.1002/sml.201001715>
- [18] Yang X, Shi K, Zhitomirsky I, Cranston ED (2015) Cellulose nanocrystal aerogels as universal 3D lightweight substrates for supercapacitor materials. *Adv Mater* 27:6104–6109. <https://doi.org/10.1002/adma.201502284>
- [19] Zhu H, Yang X, Cranston ED, Zhu S (2016) Flexible and porous nanocellulose aerogels with high loadings of metal-organic framework particles for separations applications. *Adv Mater* 28:7652–7765
- [20] Kobayashi Y, Saito T, Isogai A (2014) Aerogels with 3D ordered nanofiber skeletons of liquid-crystalline nanocellulose derivatives as tough and transparent insulators. *Angew Chemie* 126:10562–10565. <https://doi.org/10.1002/anie.201405123>
- [21] Beck S, Bouchard J, Berry R (2012) Dispersibility in water of dried nanocrystalline cellulose. *Biomacromolecules* 13:1486–1494. <https://doi.org/10.1021/bm300191k>
- [22] Eyley S, Thielemans W (2011) Imidazolium grafted cellulose nanocrystals for ion exchange applications. *Chem Commun* 14:4177–4179
- [23] Tingaut P, Zimmermann T, Sèbe G (2012) Cellulose nanocrystals and microfibrillated cellulose as building blocks for the design of hierarchical functional materials. *J Mater Chem* 22:20105–20111. <https://doi.org/10.1039/c2jm32956e>
- [24] Rosilo H, Kontturi E, Seitsonen J et al (2013) Transition to reinforced state by percolating domains of intercalated brush-modified cellulose nanocrystals and poly(butadiene) in cross-linked composites based on thiol – ene click chemistry. *Biomacromolecules* 14:1547–1554
- [25] Yang X, Cranston ED (2014) Chemically cross-linked cellulose nanocrystal aerogels with shape recovery and super-absorbent properties. *Chem Mater* 26:6016–6025
- [26] Smeets NMB, Bakaic E, Patenaude M, Hoare T (2014) Injectable and tunable poly(ethylene glycol) analogue hydrogels based on poly(oligoethylene glycol methacrylate). *Chem Commun* 50:3306–3309. <https://doi.org/10.1039/c3cc48514e>
- [27] Buesch C, Smith SW, Eschbach P et al (2016) The microstructure of cellulose nanocrystal aerogels as revealed by transmission electron microscope tomography. *Biomacromol* 17:2956–2962. <https://doi.org/10.1021/acs.biomac.6b00764>
- [28] Abraham E, Weber DE, Sharon S et al (2017) Multifunctional cellulosic scaffolds from modified cellulose nanocrystals. *Multif ACS Appl Mater interfaces* 9:2010–2015. <https://doi.org/10.1021/acsami.6b13528>
- [29] Fumagalli M, Sanchez F, Boisseau M, Heux L (2013) Gas-phase esterification of cellulose nanocrystal aerogels for colloidal dispersion in apolar solvents. *Soft Matter* 9:11309–11317. <https://doi.org/10.1039/c3sm52062e>
- [30] Rahbar K, Heidari H, Rashidi A (2016) Preparation and evaluation of nanocrystalline cellulose aerogels from raw cotton and cotton stalk. *Ind Crop Prod* 93:203–211. <https://doi.org/10.1016/j.indcrop.2016.01.044>
- [31] Chau M, De France KJ, Kopera B et al (2016) Composite hydrogels with tunable anisotropic morphologies and mechanical properties. *Chem Mater* 28:3406–3415. <https://doi.org/10.1021/acs.chemmater.6b00792>
- [32] Seifried B (2010) Physicochemical properties and microencapsulation process development for fish oil using supercritical carbon dioxide. Ph.D. Thesis, Univ. Alberta, 2010
- [33] Seifried B, Temelli F (2012) Supercritical fluid drying of high molecular weight biopolymers for particle formation and delivery of bioactives. Oral Present. 10th International Meeting on Supercritical Fluids (ISSF), May 13–16, 2012, San Fr. CA, USA
- [34] Seifried B (2016) PGX Technology: An enabling technology for generating biopolymer fibrils, particles, aerogels and nano-composites. Oral Present. 15th European Meeting on Supercritical Fluids (EMSF), May 8–11, 2016, Essen, Germany
- [35] Temelli F, Seifried B (2016) Supercritical fluid treatment of high molecular weight biopolymers. US Patent 9,249,266, U.S. Patent Trademark Off. (“USPTO”), 2011, pp 1–62
- [36] Sun B, Hou Q, Liu Z, Ni Y (2015) Sodium periodate oxidation of cellulose nanocrystal and its application as a paper wet strength additive. *Cellulose* 22:1135–1146. <https://doi.org/10.1007/s10570-015-0575-5>
- [37] Isogai A, Saito T, Fukuzumi H (2011) TEMPO-oxidized cellulose nanofibers. *Nanoscale* 3:71–85
- [38] Beck S, Méthot M, Bouchard J (2015) General procedure for determining cellulose nanocrystal sulfate half-ester content by conductometric titration. *Cellulose* 22:101–116. <https://doi.org/10.1007/s10570-014-0513-y>
- [39] Campbell SB, Patenaude M, Hoare T (2013) Injectable Superparamagnets: highly elastic and degradable poly(N-isopropylacrylamide) – superparamagnetic iron oxide nanoparticle (SPION) composite hydrogels. *Biomacromolecules* 14:644–653
- [40] Fraschini C, Chauve G, Bouchard J (2017) TEMPO-mediated surface oxidation of cellulose nanocrystals (CNCs). *Cellulose* 24:2775–2790. <https://doi.org/10.1007/s10570-017-1319-5>
- [41] Seifried B, Temelli F (2010) Density of carbon dioxide expanded ethanol at (313.2, 328.2, and 343.2) K. *J Chem Eng Data* 55:2410–2415. <https://doi.org/10.1021/je900830s>

- [42] Bhattacharjee S (2016) Review article DLS and zeta potential—What they are and what they are not? *J Control Release* 235:337–351. <https://doi.org/10.1016/j.jconrel.2016.06.017>
- [43] Reid MS, Villalobos M, Cranston ED (2017) Benchmarking cellulose nanocrystals: from the laboratory to industrial production. *Langmuir* 33:1583–1598. <https://doi.org/10.1021/acs.langmuir.6b03765>
- [44] Lyons WJ (1941) Crystal density of native cellulose. *J Chem Phys* 9:377–378. <https://doi.org/10.1063/1.1750914>
- [45] Ravikovitch PI, Neimark AV (2001) Characterization of micro- and mesoporosity in SBA-15 materials from adsorption data by the NLDFT method. *J Phys Chem B* 105:6817–6823. <https://doi.org/10.1021/jp010621u>
- [46] Seligman AM, Wasserhug HL, Hanker JS (1966) A new staining method (OTO) for enhancing contrast of lipid droplets in osmium-tetroxide-fixed tissue osmiophilic thiocarbonylhydrazide (TCH). *J Cell Biol* 30:424–432
- [47] Cherhal F, Cousin F, Capron I (2015) Influence of charge density and ionic strength on the aggregation process of cellulose nanocrystals in aqueous suspension, as revealed by small-angle neutron scattering. *Langmuir* 31:5596–5602. <https://doi.org/10.1021/acs.langmuir.5b00851>
- [48] Hirota M, Furihata K, Saito T et al (2010) Glucose/glucuronic acid alternating co-polysaccharides prepared from TEMPO-oxidized native celluloses by surface peeling. *Angew Chemie Int Ed* 49:7670–7672. <https://doi.org/10.1002/anie.201003848>
- [49] Jessop PG, Subramaniam B (2007) Gas-expanded liquids. *Chem Rev* 107:2666–2694. <https://doi.org/10.1021/cr040199o>
- [50] Dittmar D, Bijosono Oei S, Eggers R (2002) Interfacial tension and density of ethanol in contact with carbon dioxide. *Chem Eng Technol* 25:23–27. [https://doi.org/10.1002/1521-4125\(200201\)](https://doi.org/10.1002/1521-4125(200201)25:01<23::AID-CEAT23>3.0.CO;2-1)
- [51] Lim JS, Lee YY, Chun HS (1994) Phase equilibria for carbon dioxide-ethanol-water system at elevated pressures. *J Supercrit Fluids* 7:219–230. [https://doi.org/10.1016/0896-8446\(94\)90009-4](https://doi.org/10.1016/0896-8446(94)90009-4)
- [52] Takishima S, Saiki K, Arai K, Saito S (1986) Phase equilibria for CO₂-C₂H₅OH-H₂O system. *J Chem Eng Jpn* 19:48–56. <https://doi.org/10.1252/jcej.19.48>
- [53] Yao S, Guan Y, Zhu Z (1994) Investigation of phase equilibrium for ternary systems containing ethanol, water and carbon dioxide at elevated pressures. *Fluid Phase Equilib* 99:249–259. [https://doi.org/10.1016/0378-3812\(94\)80035-9](https://doi.org/10.1016/0378-3812(94)80035-9)
- [54] Yoon JH, Lee H, Chung BH (1994) High pressure three-phase equilibria for the carbon dioxide-ethanol-water system. *Fluid Phase Equilib* 102:287–292. [https://doi.org/10.1016/0378-3812\(94\)87081-0](https://doi.org/10.1016/0378-3812(94)87081-0)
- [55] Durling NE, Catchpole OJ, Tallon SJ, Grey JB (2007) Measurement and modelling of the ternary phase equilibria for high pressure carbon dioxide-ethanol-water mixtures. *Fluid Phase Equilib* 252:103–113. <https://doi.org/10.1016/j.fluid.2006.12.014>
- [56] Heath L, Thielemans W (2010) Cellulose nanowhisker aerogels. *Green Chem* 12:1448–1453. <https://doi.org/10.1039/c0gc00035c>
- [57] Dorris GM, Gray DG (1978) The surface analysis of paper and wood fibers by ESCA (electron spectroscopy for chemical analysis). II. Surface composition of mechanical pulps. *Cellul Chem Technol* 12:721–734
- [58] Reid MS, Villalobos M, Cranston ED (2016) Cellulose nanocrystal interactions probed by thin film swelling to predict dispersibility. *Nanoscale* 8:12247–12257. <https://doi.org/10.1039/C6NR01737A>